Forces on a Large Cylindrical Bubble in an Unsteady Rotational Flow

Mohammad Taeibi-Rahni and Eric Loth
Dept. of Aeronautical and Astronautical Engineering, University of Illinois at Urbana-Champaign, Urbana, IL 61801

The full Navier–Stokes equations were employed with a single-fluid model and a front tracking scheme to study a large cylindrical bubble in a free shear layer. A general formulation based on work by Auton et al. of the hydrodynamic forces on a finite Reynolds number large bubble in an unsteady, nonuniform and rotational flow was then used to investigate the effects of nonlinear spatial and temporal gradients on dispersion. The resulting bubble dispersion in the full Navier–Stokes solution significantly differ from that by a conventional bubble dynamic equation based on linear spatial gradients and quasi-steady flow. This was due to the adjunct forces not accounted for by such a formulation, which are related to regions of high nonuniformity and unsteadiness. These adjunct forces in the drag/lift direction were correlated with rapid variations of relative bubble velocity and high gradients of the liquid velocity.

Introduction

The hydrodynamic forces on a bubble in a turbulent flow control both the bubble dispersion and turbulence modulation. Most bubbly flow computations rely on a point bubble approximation with quasi-steady force coefficients (empirical in the case of drag). By examining a direct solution of a *large* bubble trajectory in a strongly unsteady, nonuniform, and rotational flow, one may evaluate the fidelity of classic bubble dynamic equations and determine whether significant additional force contributions are present. There are two regimes of bubbly flow where the forces not accounted for by conventional bubble momentum equations (herein referred to as *adjunct* forces) may become significant: (1) when the ratio of bubble response time to turbulence timescale (Stokes number, St), approaches unity; and (2) when the ratio of bubble diameter to the continuous phase integral scale (dispersion length scale, β) is no longer much less than one, that is, the temporal and spatial nonuniformities of the fluid are of the same order as the bubble time and length scales. For bubble Reynolds numbers (Re_B) much greater than unity, either of these two conditions may lead to modified pressure and velocity distributions around the bubble, which may, in turn, yield hydrodynamic forces significantly different from those given by the conventional quasi-steady force expressions. This is because conventional bubble dynamic equations typically assume a *point bubble* where spatial and temporal gradients are represented by assuming uniform shear (inappropriate for $\beta \sim 1$) and/or assume a Basset history force derived for Stokes flow (inappropriate for $Re_B \gg 1$). The Basset history term represents the effect of the history of the relative acceleration (Odar and Hamilton, 1964), and its importance is typically small for high Reynolds number bubbles with $\beta \ll 1$ (Sridhar and Katz, 1993; Mei et al., 1994) and is therefore typically neglected. However, it is likely to be important for St and/or $\beta \sim 1$. Thus, conventional bubble dynamic equations may not be appropriate for either of the two stated conditions.

The former condition ($St \sim 1$) can occur when the bubble Reynolds number (Re_B) is large enough that the drag coefficient (C_D) no longer follows the Stokesian form and becomes nearly constant yielding a Stokes number directly proportional to β (Cebrzynski and Loth, 1994). The latter condition (β not $\ll 1$) obviously results when the bubble diameter is no longer a very small fraction of the interacting free shear structures, which can occur in sudden expansion pipe flows. Even for flows for which the global St or $\beta \ll 1$, we may find regions of significant velocity fluctuations for which the local eddies yield a *local* St or β of order one. For example, the high Reynolds number turbulent shear flows yield strong small-scale structures (Oakley et al., 1994). Similarly, in a large eddy simulation (LES) of a bubbly flow, the bubbles

may be of significant size with respect to the subgrid (unresolved) turbulence scales. Finally, in a flow with many bubbles, a bubble cloud may be formed, which tends to behave in some respects as a single large bubble, albeit at a lower density ratio. It should also be noted that for the large bubbles of β and St of order unity, the effective Weber number may result in significant deformation yielding an additional complexity that can strongly modify the bubble hydrodynamics (Bhaga and Weber, 1981) but will not be considered in this study in order to simplify the fluid physics.

Previous computational studies

Numerical simulations of two-phase flows can be considered with mixed-fluid, separated-fluid, or single-fluid models (Faeth, 1987). These three different treatments of the dispersed phase refer to neglect of velocity differences, use of a point mass treatment, or use of a finite-size dispersed phase in the flow field, respectively. *Mixed-fluid* models neglect relative velocity differences and simply treat the flow as a variable-density mixture. *Separated-fluid* models allow relative velocity differences by treating the dispersed phase as a *point mass* and typically employ quasi-steady expressions for the bubble hydrodynamic forces (see next section). Recent research (e.g., Ruetsch and Meiburg, 1993; Tio et al., 1993), employing point bubble dispersion using a separated-fluid model, has demonstrated that small bubbles ($St \ll 1$) follow the vortex structure as tracers, that very large bubbles ($St \gg 1$) are unaffected by the large-scale structure, and that intermediate size bubbles (St of order 1) are most likely to be entrapped in the vortices. Thus, St directly influences the coupling between bubble dispersion and eddy structures.

The third treatment is a *single-fluid* model that allows direct description of the displacement and wake effects and eliminates the need for employing empirical or Stokesian quasi-steady expressions for added mass, drag, and lift (Taeibi-Rahni et al., 1994). Such a model either computes the ambient fluid field around the physical boundary of the discrete dispersed phase (as in the case of a solid particle) or also within the dispersed phase itself (as in the case of a droplet or bubble, where internal flow is also important). This model is usually used when the length scale of the dispersed phase is significant, compared with an integral length scale of the continuous phase, since the resulting interaction with the continuous phase can no longer be considered to act at a single point of the flow field. To the authors' knowledge, there have been no previous single-fluid numerical studies that describe the hydrodynamic forces of large bubbles, that is, β and St of order unity, in a nonlinear free shear flow.

Bubble dynamic equations

Maxey and Riley (1983) derived an equation for the forces on a small rigid sphere in an unsteady nonuniform flow, but limited to *Stokesian* flow conditions, which included buoyancy, stress gradient, Stokes drag, and Basset history terms as well as Faxen effects. Using a different approach, Auton et al. (1988) derived a formulation for forces on a body of simple shape moving through an inviscid fluid that is unsteady, nonuniform, and rotational. They assumed that the body's radius of curvature was small compared with the scale over which the strain rate changes ($\beta \ll 1$) and their equation included buoyancy, stress gradient, and inviscid lift. This resulted in lift coefficients of 2 and 1/2 and added mass coefficients of 1 and 1/2 for cylinder and sphere geometries, respectively. Comparison of Auton's and Maxey-Riley's equations shows that the Faxen, Basset, and viscous effects have been neglected by Auton and that the added mass term is slightly different due to Auton's inviscid flow assumption. On the other hand, Auton's equation is not limited to either spherical geometries or Stokesian flows.

Modifications of the force expressions used in bubble dynamic equations have been the subject of much experimental and theoretical research (e.g., Kuo and Wallis, 1988; Yang and Leal, 1991; Jiang et al., 1993; and Sangani and Didwania, 1993). In addition, Mei et al. (1991) used a single-fluid model to investigate the drag component related to the Basset history force for small-amplitude fluctuations of a *finite volume spherical* bubble at finite Re_B (about 10–100). Their findings show that this term is not always negligible and is fundamentally different for finite Reynolds numbers than that given by the Stokesian expression. Similar changes may be expected for lift component and other hydrodynamic force expressions for nonuniform unsteady flows.

Objectives

Current formulation of the hydrodynamic forces on a bubble employ many assumptions that may no longer be valid for St and β of order unity. For such bubbles, the flow encountered may be strongly *nonuniform* (in both velocity and vorticity) and *unsteady*. Therefore, this study has two main objectives: (1) to note the predictive ability of conventional bubble dynamic equations for such conditions; (2) to determine the significance and general nature of the additional forces not accounted for when using classic quasi-steady expressions for drag and lift, referred to herein as "adjunct forces." To study the significance of these adjunct forces, we observed finite Reynolds number large cylindrical bubbles subjected to an unsteady, nonuniform, and rotational flow given by a nonlinear free shear layer. The proposed study is unique in that it examines a *large* bubble in a strongly fluctuating field for which details of the nonempirical bubble motion (position, velocity, acceleration, etc.) and of the surrounding liquid fluctuation (velocity, vorticity, acceleration, divergence, etc.) are available.

Numerical Method

Computation of liquid and bubble flow field

In this study, a *single-fluid* model is employed to allow direct description of the displacement and wake effects by simulating the flow around and inside the bubble, where a front-tracking algorithm is employed to prescribe the interphase boundary (Unverdi and Tryggvason, 1992). The flow is computed with the unsteady, incompressible, viscous, immiscible, multifluid, two-dimensional Navier–Stokes equations for the liquid and the gas, where the momentum equations in conservative form are:

$$\frac{D(\rho V)}{Dt} = -\nabla p + \rho g + \nabla\cdot(2\mu T) + \sigma\kappa n\,\delta(X - X^f), \quad (1)$$

where T is the rate of deformation tensor with components: $T_{ij} = (V_{i,j} + V_{j,i})/2$; V is the velocity vector (liquid and the gas); σ is the surface tension coefficient; κ is the radius of curvatures; g is the gravity acceleration; and n is a normal to the bubble surface. The numerical scheme used is a relatively standard finite difference projection method that is second order in space and time, where the implicit pressure equation is solved by a successive overrelaxation technique (Unverdi and Tryggvason, 1992; Taeibi-Rahni, 1995). Two separate grid systems are used: (1) a fluid grid that is structured, two-dimensional, staggered, and of uniform discretization in both dimensions; and (2) a front grid that is unstructured, adaptive, and one-dimensional and embedded in the fluid grid. The density (ρ) and the viscosity (μ) are varied such that they are constant on either side of the bubble and vary monotonically through the bubble front using a smoothened interface function distributed along the front with a thickness limited to four fluid grid cells (Unverdi and Tryggvason, 1992). The surface tension forces and the interface function have been added as a delta function, $\delta(X - X^f)$, which is nonzero only on the finite thickness bubble surface, where $X = X^f$. The one-dimensional front grid is advected by the fluid velocity, which is interpolated from the fluid grid. An example of the structured grid resolution and the front with respect to the flowfield is shown in the results section. The resulting single-fluid equations are therefore valid for the whole two-phase flow (both the bubble and the ambient liquid flow fields) and allow removal of any quasi-steady (empirical) hydrodynamic force coefficients. Thus, during the time-accurate trajectory of the bubbles as they encounter large-scale eddies and braids, the unsteady and flow gradient effects on all the bubble hydrodynamic forces are intrinsically taken into account. We therefore refer to this fully resolved computation as a direct numerical simulation (DNS).

Computation of bubble hydrodynamic forces

Once the preceding time-varying flow field and history of the bubble characteristics were obtained, we applied the following methodology *a posteriori* to determine the adjunct forces that include additional effects of nonlinear spatial and temporal flow gradients. Auton's bubble dynamic equation mentioned earlier is herein generalized to include drag and adjunct forces:

$$(\rho_B + \rho_L C_m)\mathrm{Vol}_B \frac{dV_B}{dt} = \mathrm{Vol}_B(\rho_B - \rho_L)g + D'_{QS} + L'_{QS} + \mathrm{Vol}_B\left\{\rho_L\left[(1 + C_m)\frac{DV_L}{Dt}\right]\right\} + A', \quad (2)$$

where

$$\frac{d(\,)}{dt} = \frac{\partial(\,)}{\partial t} + V_B \cdot \nabla(\,) \quad (3)$$

and

$$\frac{D(\,)}{Dt} = \frac{\partial(\,)}{\partial t} + V_L \cdot \nabla(\,) = \frac{d(\,)}{dt} - (V_B - V_L)\cdot\nabla(\,). \quad (4)$$

In Eq. 2, the forces on the righthand side are buoyancy, quasi-steady drag, and lift; the force resulting from the stress gradients of the liquid flow in the absence of a bubble; and the adjunct force, respectively (primes indicate forces that have not been normalized). As noted by Maxey and Riley (1983), the stress gradient term includes both pressure and viscous stress gradients acting on the bubble. The "adjunct" forces represent any other forces not unaccounted for by the rest of the terms in the conventional bubble dynamic equation given earlier and arise due to the strong *unsteadiness* and *nonuniformity* of the surrounding flow, for example, the *Basset history* and the *Faxen* effects. All these forces equate to the bubble mass and the added mass times the bubble acceleration on the lefthand side. Using conventional drag and lift expressions (to be given below), the adjunct forces in the drag and lift direction were determined. Note, flow quantities were calculated following the bubble (in a Lagrangian manner), and therefore the substantial derivative in Eq. 3, $d(\,)/dt$, was found directly. Once the evolution of the adjunct force is determined for several cases, the statistical correlations of its components in the drag and lift directions were examined with respect to different bubble characteristics and liquid flow quantities.

Using the modified drag expression of a solid body, the quasi-steady drag on a bubble per unit depth can be written as

$$D'_{QS} = -k_D C_{DQS}\rho_L d_B |V_{\mathrm{rel}}| V_{\mathrm{rel}}/2, \quad (5)$$

where k_D is the ratio of drag coefficient of a fluid body to that of a solid body, subscript B signifies values with respect to the bubble centroid, and subscript L signifies the liquid outside the bubble. For the quasi-steady lift per unit depth, the following formulation (Auton et al., 1988) is used:

$$L'_{QS} = -C_{LQS}\rho_L(\pi d_B^2/4)(V_{\mathrm{rel}} \times \omega)_{\mathrm{ave}}, \quad (6)$$

where ω is the average vorticity of the liquid around the bubble and V_{rel} is defined in the following.

Since the bubble was *not* treated as a point mass, a spatial averaging of the liquid velocity and flow gradients is necessary in applying Eq. 2. For example, the average liquid velocity around the bubble, $(V_L)_{\mathrm{ave}}$, is herein obtained by integrating the DNS ambient fluid velocity in a region close to the bubble (similar to Soo, 1976). For the finite bubble Reynolds numbers of this study, for example, 50, a cylindrical bubble is influenced in an approximately inviscid manner by the ambient flow, that is, with a $1/r^2$ dependence. Therefore, the area integration was employed within the region of one to three diameters away from the bubble centroid (defined as Vol) to avoid the bubble boundary layer. Thus, the averaged value of a flow parameter, say q, for which the bubble was considered immersed, was taken as

$$q_{\mathrm{ave}} = \int_{\mathrm{Vol}} \frac{q(r)}{r^2} d(\mathrm{Vol}) \Big/ \int_{\mathrm{Vol}} \frac{1}{r^2} d(\mathrm{Vol}). \quad (7)$$

The bubble velocity relative to the average flow velocity in the vicinity of the bubble, V_{rel}, is then taken to be $V_B - (V_L)_{\mathrm{ave}}$.

Note the use of larger integration areas did not significantly affect the force calculations of this study (Taeibi-Rahni, 1995). Finally, recall that the bubble trajectories (and therefore the velocity and acceleration of its centroid) are determined nonempirically from the DNS computations, *while Eq. 2 was only used afterwards to solve for the adjunct forces.*

Large Cylindrical Bubble in a Planar Free Shear Layer

In this study, two-dimensional direct numerical simulations of a large cylindrical bubble and its surrounding flow field immersed in a temporally developing shear layer was completed with minimal bubble deformation and without resorting to use of quasi-steady hydrodynamic force coefficients (e.g., C_D and C_L). The two-dimensional shape bubble was chosen since it allows high spatial resolution, has been investigated both experimentally and numerically by several researchers (e.g., Shankar, 1992; Auton et al., 1988), and contains all the general characteristics of the spherical counterpart. The minimal deformation condition is in order to allow focus on the fundamental changes caused by the effects of nonlinear spatial and temporal gradients on the bubble hydrodynamics. It is a prescribed physical limitation, not a computational restriction, as evidenced by the highly deformed simulations by Unverdi and Tryggvason (1992) and Taeibi-Rahni (1995) with the same scheme.

Test conditions

A planar free shear layer was selected as the continuous phase because it is a canonical flow and its eddy structure is more coherent and accessible than other shear flows. Inserting large bubbles (β and St of order unity) in such a flow permits clear evaluations of the bubble dispersion by the shear layer's coherent structures. To obtain a representation of this bubbly shear layer flow, the computational effort included a DNS of one or two cylindrical bubbles embedded in a *finite Reynolds number* shear layer with $Re_{\delta 0} \equiv \rho_L \Delta u \delta_0 / \mu_L = 250$, where δ is the streamwise averaged shear layer thickness based on the 5% and 95% levels of the mean velocity profile, and Δu is the velocity difference across the shear layer. At such Reynolds numbers, the small-scale turbulent structure and three-dimensionality associated with a fully developed turbulent flow at higher Reynolds numbers are notably *absent*, but the nonlinear spatial and temporal gradients will still be pronounced. Therefore, this unsteady, nonuniform and rotational flow field coupled with the finite Reynolds number bubble contains many of the aspects associated with actual large bubbles in a complex turbulent field.

Temporal free shear layer development, which was based on periodic boundary conditions for the left and right boundaries and *full slip* conditions for the top and bottom walls, was employed in this study (for details, see Taeibi-Rahni, 1995, and Taeibi-Rahni et al., 1994). A perturbation using a harmonic wavenumber (w_f) and a 90° out-of-phase subharmonic ($w_s = w_f/2$) superimposed on a hyperbolic tangent mean profile was employed based on the results of Metcalfe et al. (1987) to yield the fastest vortex pairing. This yields uniform velocity fields above and below the initial disturbance of $u_1 (= 2)$ and u_2 $(= -u_1 = -\Delta u/2)$. Note in this study all length scales were normalized by the initial vorticity thickness, $\delta_{\omega 0} (\equiv u_1/[\partial u/\partial y]_{0,\ \max})$, and all velocity scales were normalized by $u_1/2$, where subscripts 1 and 2 here signify the conditions far above and far below the shear layer, respectively. In order to yield two full fundamental waves, a flow domain of width of $4\pi/w_f$ and height of $8\pi/3w_f$ was used. Gravity (when added) is in the streamwise direction, indicating a vertical shear layer for which buoyancy would direct the bubbles parallel to the shear layer.

Test conditions for the flow simulations were chosen based on a modest variation of parameters and effects presumed to be important in studying bubble dynamics, in order to help differentiate influence of these various effects. The resulting bubble dispersion was investigated by varying parameters for the five cases shown in Table 1. In the shear layer cases, we first investigated the effect of only fluid displacement by just adding surface tension (case D), then added the centripetal effect by changing the bubble density (case E), and finally added buoyancy by setting gravity to be nonzero (cases F–H). In the rising bubble cases (A and B) all effects were present. In all cases, a minimal bubble deformation was achieved by choosing a sufficiently high surface tension coefficient ($\sigma = 40$), although low deformation was not a computational restriction. For cases E–H, a ρ_L/ρ_B of 40 was used since higher ratios did not lead to significant changes in the flow but significantly increased computational time (Taeibi-Rahni, 1995). For the *rising bubble* studies (cases A and B), g values of 0.2 and 0.7 were used, corresponding to theoretical bubble terminal Reynolds numbers (Re_t) of 65 and 133, while the bub-

Table 1. Bubble and Flow Properties for Cases A–H

Cases	Bubble Initial Position	ρ_L/ρ_B	g	V_t Theoret.	V_t Comput.	$St^* \equiv \tau_B/\tau_L$ (Terminal/Relative)	$Fr_{\delta 0}^{\dagger} \equiv \Delta u^2/4g\delta_0$	$\xi \equiv (\Delta u/V_t)^2$
A (rising bubble)	—	40	0.20	0.76	0.84	—	—	0
B (rising bubble)	—	40	0.70	1.58	1.70	—	—	0
C (single-phase)	—	1	0	—	—	—	—	—
DL (two-phase; σ only)	Left	1	0	—	—	0.0/20.58	∞	—
DR (two-phase; σ only)	Right	1	0	—	—	0.0/11.71	∞	—
E (two-phase; $\Delta\rho$ added)	Right	40	0	—	—	0.0/2.59	∞	—
F (two-phase; g added)	Right	40	0.02	0.19	0.21	8.67/4.08	51	711
G (two-phase; g added)	Left	40	0.20	0.76	0.84	3.42/4.65	5	20
H (two-phase; g added)	Left	40	0.70	1.58	1.70	1.97/2.51	1.5	5

* Stokes number is based on either theoretical terminal velocity or average relative velocity.
† Subscript 0 signifies $t = 5$, when bubble(s) was initially introduced into the mixing layer.

bles in the free shear layer flows employed a range of gravity values ($g = 0$, 0.02, 0.2, and 0.7). The combination of the preceding gravities, density ratios, and initial shear layer profile resulted in conditions where centripetal and buoyancy forces could be significant as compared to drag.

For the Stokes number (St) defined earlier, the bubble timescale is the bubble mass and the apparent (or added) mass times the relative velocity divided by the quasi-steady drag force; whereas the shear layer timescale was defined as the average shear layer thickness divided by the velocity difference across the shear layer (Δu), yielding $St = \pi(\rho_B + C_m \rho_L) d_B \Delta u / 2 \rho_L k_D C_{DQS} |V_{rel}| \delta$. Table 1 shows St for each case based on either theoretical terminal velocity or average $|V_{rel}|$ from $t = 5$—25 (except case H which was terminated at $t = 20$). The dispersion length scale, β, is defined herein as the ratio of the bubble diameter (d_B) to the mixing layer thickness (δ), where β_0 was always 0.83 in this study. Also shown in Table 1 are two other ratios related to competing mechanisms: the ratio of the centripetal pressure gradient to the buoyancy pressure gradient (*Eddy Froude number*, Fr_δ), and the ratio of convection to buoyancy forces (*convection-buoyancy ratio*, ξ). These parameters are defined for a two-dimensional bubble in a free shear layer as: $Fr_\delta = \Delta u^2/(4\delta g)$ and $\xi = (\Delta u / V_t)^2$ (Taeibi-Rahni et al., 1994). In cases F, G, and H, where gravity is present, the pressure gradient in the eddy radial direction is initially higher than that in the gravity (streamwise) direction, and the chances are high that a bubble moving close to an eddy will be at least temporarily attracted.

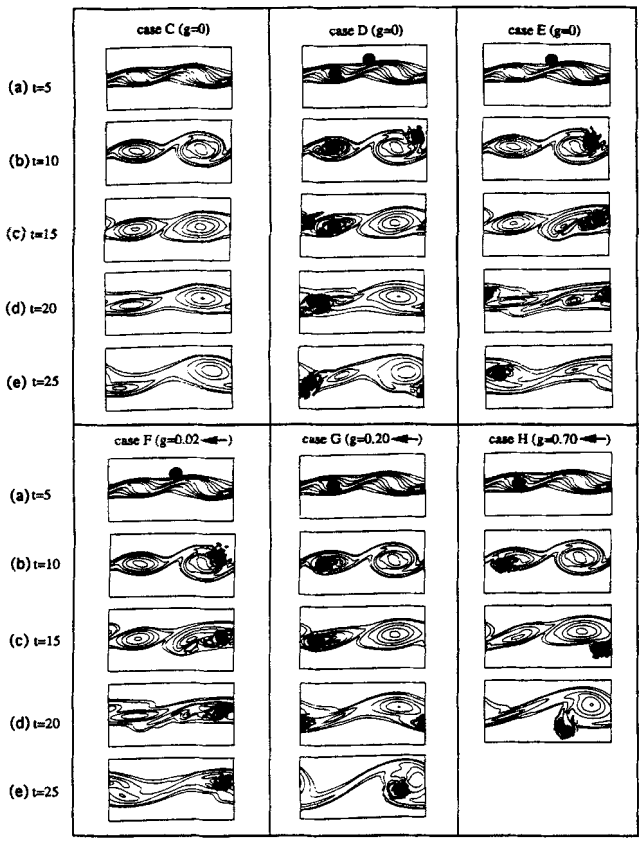

Figure 1. Evolution of vorticity contours for cases C (single-phase), D (both core and braid bubbles with $\rho_B = \rho_L$ and $g = 0$), E (braid bubble with $\rho_B \ll \rho_L$ and $g = 0$), F (braid bubble with $\rho_B \ll \rho_L$ and $g = 0.02$), G (core bubble with $\rho_B \ll \rho_L$ and $g = 0.2$), and H (core bubble with $\rho_B \ll \rho_L$ and $g = 0.7$).

For the shear layer, the bubble was added at $t = 5$ by simply providing an instantaneous change to the density and viscosity fields as well as addition of surface tension, while retaining the original velocity and hydrodynamic pressure fields of the shear layer, that is, mass was instantly withdrawn to create a bubble in instantaneous velocity equilibrium. As shown in Figure 1, at $t = 5$ the initial bubble placement in the shear layer was either in the vortex core (left bubble) or on top of the connecting braid (right bubble). By this time, the free shear layer had already begun to evolve and two large eddies and a middle braid had developed due to Kelvin–Helmholtz instability. No significant flow modulation followed this instantaneous bubble addition, but later the flow field was modified whenever the bubble cut across a braid or an eddy (Taeibi-Rahni et al., 1994).

To determine numerical errors due to finite spatial and temporal resolution, several single-phase and two-phase tests were conducted by comparing results with double and half the resolution for both the single-phase and two-phase simulations. Velocity and vorticity distributions were used to investigate changes due to varying the cell Reynolds number ($Re_{cell} \equiv \rho_L \Delta u \Delta x / \mu_L$). The results indicated that the maximum local velocity difference was limited to less than 2% of Δu between the highest resolution and the baseline resolution of $Re_{cell} = 24$ (Taeibi-Rahni, 1995; Taeibi-Rahni et al., 1994). The corresponding difference in average variance between the vorticity fields (a very sensitive flow indicator) was about 2% of the maximum vorticity (Taeibi-Rahni et al., 1994). Based on these findings for a baseline resolution with $Re_{cell} = 24$, a rectangular 144×96 grid was used for all the test conditions reported herein. All computations were completed on a Cray YMP, which required approximately 1 CPU hour and 0.5 MW of core memory (Taeibi-Rahni, 1995).

Quasi-steady hydrodynamic coefficients

The treatment of Eq. 2 is qualified herein for a two-dimensional cylindrical bubble. The quasi-steady drag coefficient for flow over a solid cylinder (C_{DQS}) was taken to be $1 + 10\, Re_B^{-2/3}$, valid for $1 < Re_B < 2 \times 10^5$ as per White (1991). Since k_D of Eq. 5 for a cylinder cannot be found analytically even for Stokesian flows (Stokes paradox), it was estimated as the 2/3 factor found for a sphere (Sherman, 1990). To check the validity of this for a fluid, the computed quasi-steady drag and the total drag as well as the adjunct force in the drag direction are plotted vs. time in Figure 2 for a bubble rising flow (case B). Note that the forces (per unit depth of cylinder) in this study were normalized by $[\rho_L (\Delta u)^2 d_B / 2]$, where Δu (which is constant) has been used rather than $|V_{rel}|$ in order to better observe the relative magnitude of the forces. In this figure, the adjunct force in the drag direction behaves like a perturbation quantity (after an initial period) and averages to roughly zero, indicating that the quasi-steady expression for the drag coefficient is reasonable (similar behavior was also seen for case A). We can also investigate the appropriateness of Eq. 7 for this flow by comparing V_B and V_{rel}

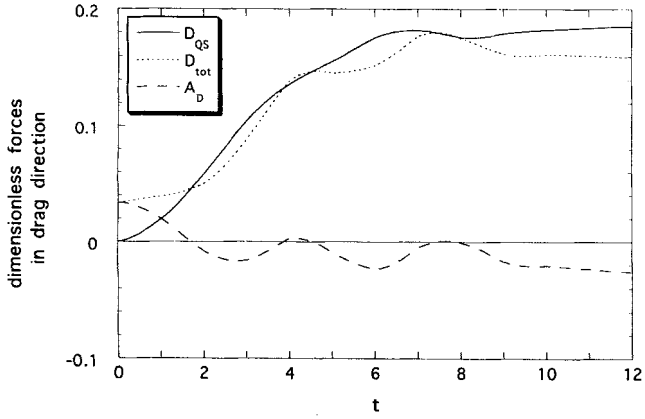

Figure 2. Bubble normalized quasi-steady and total drag forces, as well as adjunct force in the drag direction vs. time for case B (rising bubble; high gravity).

(which should be equal for rising bubble flows). For the same rising bubble case, the influence of bubble wake leads to a V_{rel} that is always less than 2% below V_B, indicating that Eq. 7 is reasonable for this flow. Based on the V_{rel} uncertainty and those associated with spatial and temporal resolution of the finite difference method, the overall uncertainty in the predicted lift and drag forces is estimated to be 15% (Taeibi-Rahni, 1995).

Lift and added mass coefficients were prescribed as given by Auton et al. (1988), where for a cylinder moving in a two-dimensional flow $C_{LQS} = 2$ and $C_m = 1$. It should be noted that C_m is not necessarily constant and in general varies with acceleration number, which is the ratio of convective acceleration to local bubble acceleration (Odar, 1964). However, only marginal differences in adjunct forces were noted in this study when the variable C_m of Odar (1964) was used as opposed to the baseline solution with $C_m = 1$. Finally, the terms for buoyancy and stress gradient given by Eq. 2 are qualified for a perfect cylinder by simply setting Vol_B per unit depth as $\pi d_B^2/4$.

DNS flow field results

The resulting DNS flow calculation showed that the bubble wake was significantly affected by the nonlinearities of the shear layer. For example, Figure 3a shows the DNS computations of a two-dimensional bubble rising in a quiescent flow at $Re_B \sim 50$, while Figure 3b shows a bubble at about the same Re_B, but in the nonlinear shear flow with a dispersion length scale (β) and Stokes number (St) of order one. This latter condition is consistent with the natural frequency of the bubble wake approaching that of the surrounding shear flow, and the result is a modified wake field. In such a case, a quasi-steady drag coefficient that only depends on Reynolds number is not appropriate for predicting the instantaneous total drag forces. Note in these figures, the velocity vector spacing is based on the actual fluid grid resolution used and where the one-dimensional front is indicated by density contours for which typical deformation levels in any direction can be seen to be less than 2% of the bubble diameter. Figure 1 shows the bubbles (as solid black circles) and vorticity

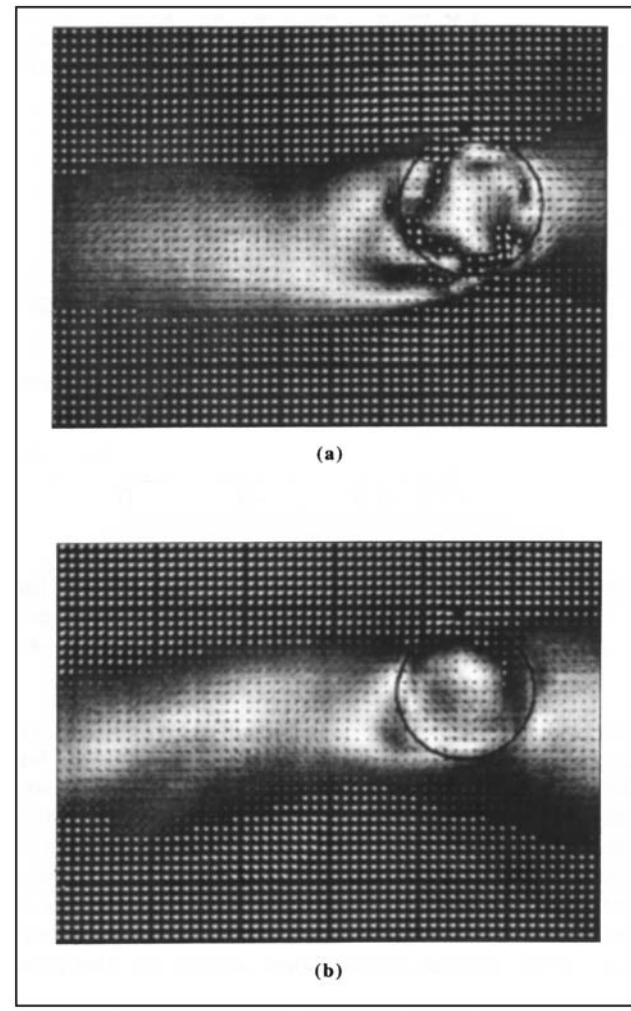

Figure 3. Bubble flow velocity vectors *relative* to the bubble centroid velocity.

This shows flow distribution around and within a bubble (a) rising in a quiescent flow at $Re_B \sim 50$ (corresponding to $t = 15$ for case A), and (b) in a nonlinear shear flow with a Stokes number (St) and dispersion length scale (β) of order one and also at $Re_B \sim 50$ (corresponding to $t = 15$ for case E). Note grey-scale shading is proportional to velocity vector magnitude and density gradients specified by the one-dimensional front are indicated with contour lines.

contours at several times for cases C–H, where the bubbles are seen to move in a complex fashion as they encounter braids and eddies (see Taeibi-Rahni et al., 1994, for details of the flow modulation)

Large bubble and point bubble trajectories

In order to note the dispersion of the bubbles, trajectories of the fully resolved bubbles computed with the single-fluid model (large bubbles) are compared with the more conventional point bubbles, which are treated as a separated fluid of negligible displacement and advected according to quasi-steady hydrodynamic force expressions using a separated fluid model. We first discuss dispersion of the large bubbles. The rising bubble trajectories were not perfectly rectilinear due to natural oscillations of the bubbles in their trajectories, and thus the instantaneous trailing wake was typically asymmetric

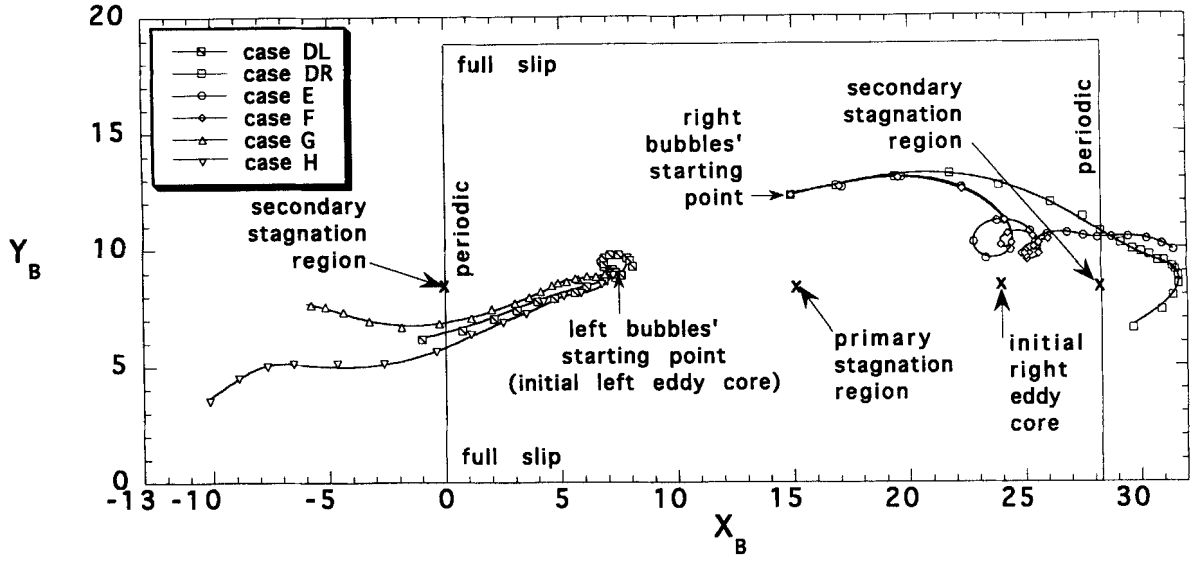

Figure 4. Trajectories of the bubbles for cases D (both core and braid bubbles with $\rho_B = \rho_L$ and $g = 0$), E (braid bubble with $\rho_B \ll \rho_L$ and $g = 0$), F (braid bubble with $\rho_B \ll \rho_L$ and $g = 0.02$), G (core bubble with $\rho_B \ll \rho_L$ and $g = 0.2$), and H (core bubble with $\rho_B \ll \rho_L$ and $g = 0.7$).

with respect to the streamwise direction at a given time. Trajectories of the absolute motion of the centroid of the bubbles for all bubbly shear layer cases are plotted in Figure 4 and range from $t = 5$ to 25 for cases D–G , and 5 to 20 for case H. Within the shear layer, the large bubble motion was much more complex since convection forces become important. Since the bubbles of cases D, E, G, and H cross the periodic boundaries (some at left and some at right), extensions of the original computational domain are also shown for clarity. Note also that the gravity (when present) is from right to left, and that the data points correspond to unit time intervals, for example, $t = 5, 6, 7$.

By comparing the trajectories with flow streamlines, it is clear that the bubbles of case D (displacement effect only) behave essentially like a passive scalar and nearly follow the motion of the surrounding liquid. This is consistent with the absence of forces pulling the bubble out of equilibrium except for a noninstantaneous response time (Table 1). For instance, the right bubble of case D passed by the right eddy without being significantly attracted toward it, but the right bubbles of cases E (displacement and centripetal effects) and F (all effects) were pulled toward their low-pressure cores due to the centripetal effects. Also note that the bubble of case E makes one big and one small loop and then leaves the right eddy, while the bubble of case F makes three small loops and at $t = 25$ is still trapped in the eddy. This looping behavior is a characteristic of intermediate Stokes number values of these bubbles (Table 1).

Comparing the trajectories of the left bubbles, the bubbles of cases G and H are pulled from the core by buoyancy, after which they are convected counterclockwise below the eddy, whereas the left bubble of case D (with no buoyancy or centripetal effects) only moves by convection and thus stays much longer in the core. The buoyancy effect for escaping the core is seen more clearly in Figure 5, which shows the trajectories of the bubbles of cases G (all effects; $g = 0.2$) and H (all effects; $g = 0.7$) with respect to a coordinate system *moving with the core of the left vortex* (defined as the maximum vorticity point). The bubbles are now clearly seen to be pulled to the *right* of the core by buoyancy, after which the lower stream velocity convects them downward and to the left. While case G with a higher Fr_δ (see Table 1) evolved at a slower rate, its buoyancy effect is sufficient for it to escape as well.

As an evaluation of the fidelity of the classic bubble dynamic equation to predict dispersion for such flows, an uncoupled *point bubble* trajectory was also computed to compare with the single-fluid model trajectories of Figure 4. For the point bubble computations, the sum of just the quasi-steady forces (no adjunct forces) was used to determine the instantaneous bubble acceleration. The bubble dynamic

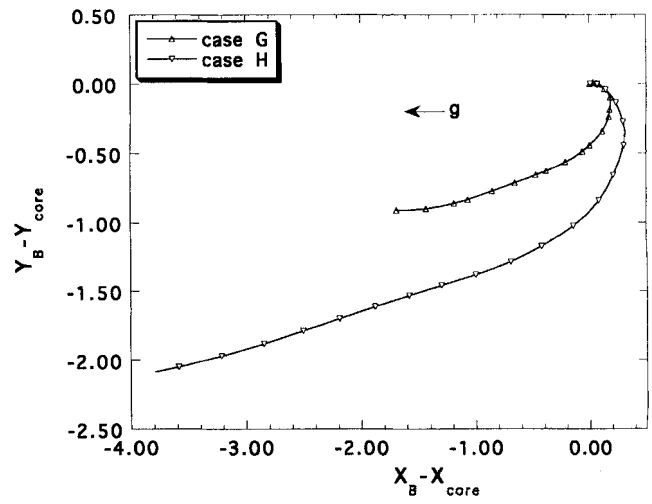

Figure 5. Relative trajectories of the bubbles with respect to the core of the eddy for cases G (core bubble with $\rho_B \ll \rho_L$ and $g = 0.2$), and H (core bubble with $\rho_B \ll \rho_L$ and $g = 0.7$).

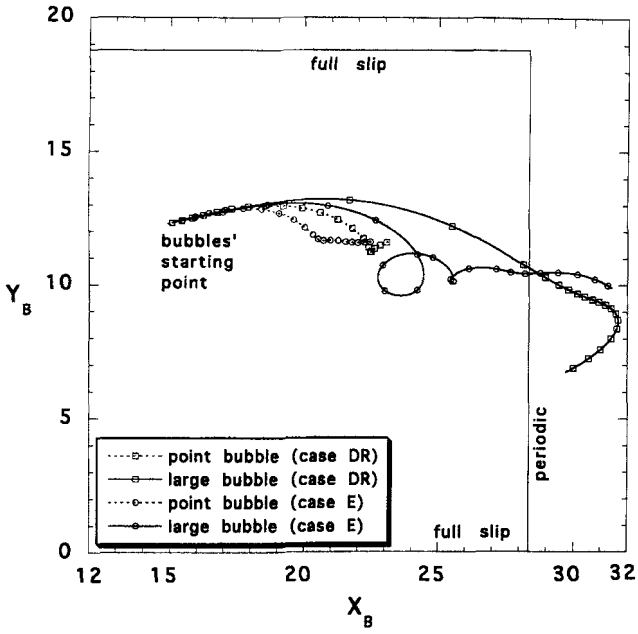

Figure 6. Trajectories of the point bubbles and fully resolved large bubbles for cases DR (braid bubble only with $\rho_B = \rho_L$ and $g = 0$) and E (braid bubble with $\rho_B \ll \rho_L$ and $g = 0$).

equation was integrated in time to find a point bubble velocity and trajectory using the results of the single-phase shear layer flow field (case C). Therefore, the point bubble velocity was determined solely by the quasi-steady forces of Eq. 2, whereas the large bubble velocity was determined by the DNS hydrodynamic forces of Eq. 1. The liquid properties [such as V_L, ∇V_L, and (dV_L/dt)] for the point bubble were spatially interpolated *a posteriori* from the single-phase flow field for each DNS time increment (as opposed to averaging over a finite domain of the bubble DNS solution, as was done in Eq. 7 for the large bubble interrogation). By using case C for the point bubble ambient fluid field, we are neglecting any flow modulation effects on the dispersion; however, this is a reasonable approximation for case D and E up to $t \sim 20$ (Figure 1). The same initial position and the same zero relative velocity used for the large bubbles for cases D and E (just above the middle primary braid) was also used for the point bubble cases to begin the trajectories at $t = 5$. Thus, the fundamentally different techniques (quasi-steady vs. DNS) for bubble dispersion can be evaluated directly.

Right bubble trajectory results are shown in Figure 6 for both the point bubble and the single-fluid (large bubble) models, from $t = 5$ to $t = 25$. For case D, the point bubble moves slower as opposed to the large bubble (both of which move faster than the surrounding liquid) because the large bubble's drag was initially much less than its quasi-steady value. This lower speed allows the point bubble to be convected downward by the right eddy. However, once it gets close enough to the core, the bubble's high relative velocity and increasing vorticity cause a rapid increase in lift in the $+y$ direction. In addition, the increased relative velocity caused by the eddy crossing results in a strong drag force component in the $+y$ direction as well, which yields a small loop just before $t = 25$.

The case E point bubble also moves slower than its large bubble counterpart for similar reasons, but due to its lower density it is pulled more toward the eddy core than the case D point bubble. Lift and drag forces eventually become strong enough to overcome the centripetal force such that its attraction toward the eddy core is diminished and the bubble convects to the right from $t = 20$ to 25 (although without a loop). In general, the point bubbles moved only about half the streamwise and transverse distances of the large bubbles and with fundamentally different trajectories in the same time period. Therefore, the effects of removing the quasi-steady assumptions of lift, drag, and added mass coefficients are now readily seen, as the single-fluid model (which assumes none of these) yields significantly different dispersion from that of the point bubble model (which assumes all of these). This is important since the point bubble approximation is widely used in many turbulent bubbly flow design codes and that a better understanding of the bubble response to strongly unsteady nonuniform flows (adjunct forces) might be useful for the bubbly flow conditions outlined in the introduction.

Evolution of bubble hydrodynamic forces

To study the bubble dynamics for the different cases, various forces acting on the bubble of each case in the drag and lift directions were investigated during their time evolution. From these, the total lift and drag fores were computed by decomposing Eq. 2 into the drag and lift directions:

$$\boldsymbol{D}_{\text{tot}} = \boldsymbol{I}_D - \boldsymbol{B}_D - \boldsymbol{S}_D \quad \text{and} \quad \boldsymbol{L}_{\text{tot}} = \boldsymbol{I}_L - \boldsymbol{B}_L - \boldsymbol{S}_L, \quad (8)$$

where $\boldsymbol{I}$ represents the actual inertial accelerations of the large bubble from the DNS solution; $\boldsymbol{B}$ represents the buoyancy force; and $\boldsymbol{S}$ represents the stress gradient force. Thus, the total drag is defined as the sum of the quasi-steady drag and the adjunct forces in the drag direction, where total lift is defined similarly. Note, only when the adjunct forces are significant will there be a large difference between total and quasi-steady values of lift and drag.

In the rising bubble cases A ($g = 0.2$) and B ($g = 0.7$), both the quasi-steady and the total drag grew monotonically until the bubble reached its terminal velocity, after which these drag forces approached nearly constant values equal to the buoyancy force (Figure 2). As expected, the quasi-steady drag predictions ($\boldsymbol{D}_{QS}$) agreed well with the total drag force ($\boldsymbol{D}_{\text{tot}}$) evolution (found from DNS) due to the quiescent character of the fluid observed by the bubble. The stress gradient drag and lift forces were relatively small, as expected, but grew slightly with time due to the growth of the bubble wake asymmetries.

The evolutions of the forces on the bubbles in the shear layer are discussed using details of two time histories (one for a left bubble and one for a right bubble) that typified the results (results for the other cases are given in Taeibi-Rahni, 1995). The evolution of the forces in the drag and lift directions for case D (displacement effect only; *left bubble*) is shown in Figure 7. Up to $t \sim 17$, this bubble is trapped in the left eddy and follows the liquid as a tracer and, therefore, forces on the bubble remain relatively small. After this time, the bubble leaves the eddy, accelerates, and arrives at the highly nonuniform secondary stagnation region (denoted in Figure

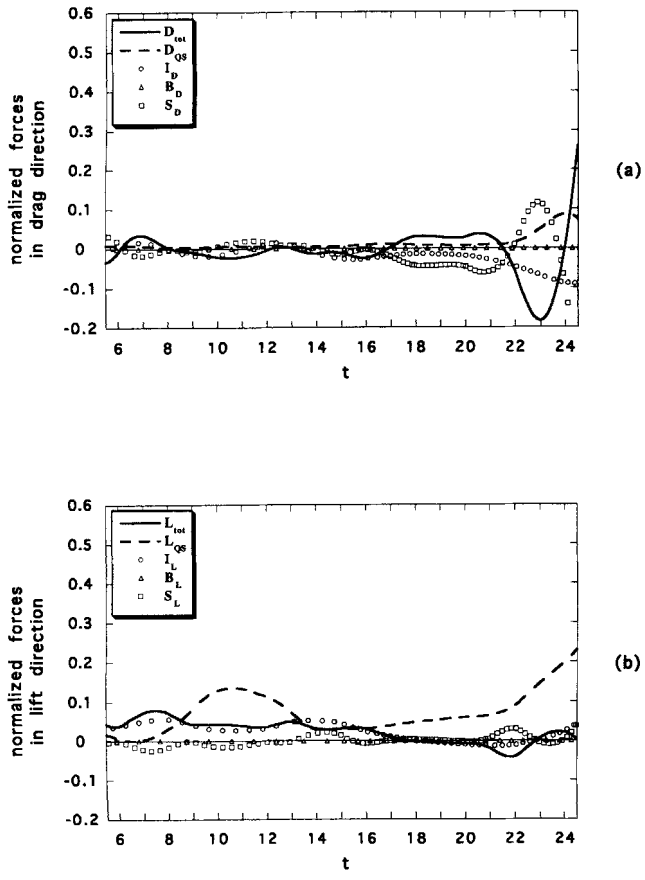

Figure 7. Evolution of different forces on the bubble of case DL (core bubble only with $\rho_B = \rho_L$ and $g = 0$) in (a) drag direction and (b) lift direction.

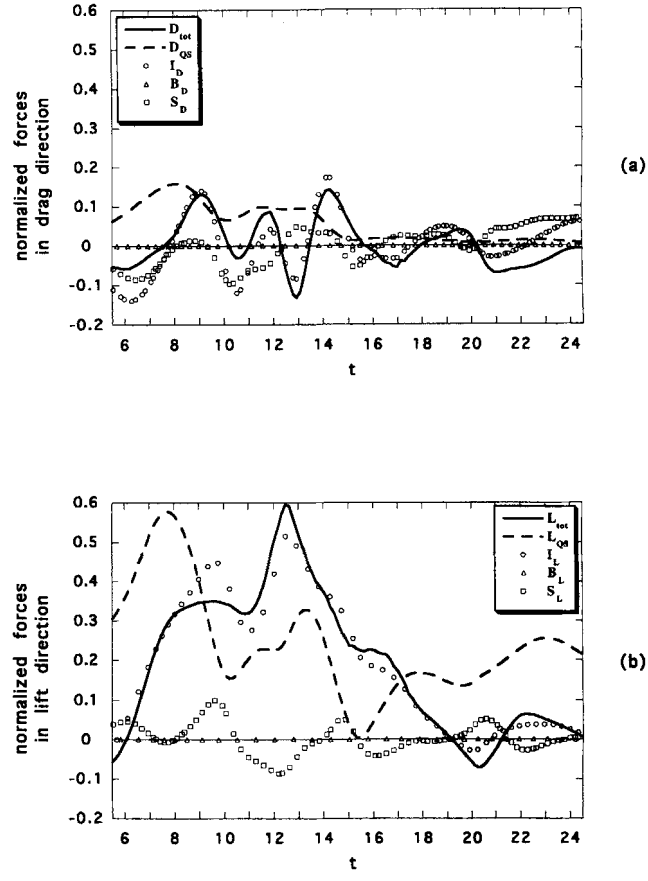

Figure 8. Evolution of different forces on the bubble of case E (braid bubble with $\rho_B \ll \rho_L$ and $g = 0$) in (a) drag direction and (b) lift direction.

4) at about $t \sim 21$, resulting in a considerable change in both quasi-steady and total drag (Figure 7a). A similar result was found when the right bubble of case D arrived there at $t \sim 12$ (Figure 4). The flow nonuniformity of the secondary stagnation region (center of the secondary braid) is evidenced by rapid increases in V_{rel} and ∇V_L, which is correlated with a high adjunct force in the drag direction. In addition, the adjunct force in the lift direction became significant after $t \sim 21$ as well, but to a more modest extent (Figure 7b). Note, the deviation between total and quasi-steady lift was not consistent with the deviation between total and quasi-steady drag; therefore, changes in the added mass coefficient cannot fully explain and are thus not primarily responsible for adjunct force significance. The left bubble of case G is only trapped in the left eddy for a short time and yields similar trends to that of case D (left bubble; Figure 7) but at higher values.

The forces in the drag and lift directions for the right bubbles of cases E (shown in Figure 8) and F, are both of similar amplitude and follow similar trends. The lift and drag forces in these two cases appear much more oscillatory compared to case D, primarily due to the loops the bubbles make in their trajectories (Figure 4). The timescale of these oscillations is also very near to that of the bubble response time of approximately 3. This oscillatory lift and drag has been also noted by Tsuboi et al. (1989) for forces on an oscillating cylinder. Similar to the right bubble of case D, the bubbles of cases E and F experience high deviations between D_{tot} and D_{QS} and also between L_{tot} and L_{QS} up to $t \sim 8$, as they approach the core of the right eddy. While in the right eddy ($8 < t < 19$ for case E and $8 < t < 25$ for case F), the adjunct drag force stays relatively small due to the decrease in the relative velocity, but because of the high accelerations in the lift direction (as a result of the looping motion), the adjunct lift force stays extremely high until the looping motion stops. After $t \sim 19$, the bubble of case E leaves the right eddy due to bouyancy and moves to the secondary stagnation region, where it again experiences increases in its adjunct drag and lift forces, presumably due to high flow nonuniformity. In general, for the cases considered in this study, bubble passage through the braid center tends to lead to high adjunct drag forces due to rapid changes in the relative velocity, whereas bubble passage through the eddy core tends to lead to high adjunct lift forces due to strong liquid stress gradients and rapid vorticity changes. We may also conclude that the total forces oscillate about their quasi-steady values, such that the adjunct forces contain strong positive and negative oscillations, but when averaged over time are small.

Unsteady drag and lift correlations

With the help of the force evolutions discussed in the previous section, the correlation of the adjunct forces are exam-

ined. Recall, A represents the forces typically unaccounted for by the point bubble approximation (see the section titled "Computation of Bubble Hydrodynamic Forces"). The following main factors contribute to the adjunct forces in the drag and lift directions given in Eq. 2: (1) added mass coefficient was assumed constant throughout this study, and (2) the models for the quasi-steady drag and lift coefficients and absence of the Basset history term and Faxen effects assume that the ambient flow velocity or at least vorticity (as seen by the bubble) is uniform ($\beta \ll 1$) and steady ($St \ll 1$). However, the complexity of the present flow allows only general and qualitative statements about how the unsteady and nonuniform flow control the adjunct forces. In an attempt to determine their overall nature, these forces were correlated with instantaneous characteristics of the immersed fluctuating flow field. Hence, several flow parameters (e.g., V_{rel}, ω, and ∇V_L) and their time derivatives were investigated for possible correlations with the adjunct forces in either the drag or lift directions. Most of these did not exhibit consistent correlations, but those that did are discussed below.

The correlation between the adjunct drag force (normalized by the quasi-steady drag) and the bubble Reynolds number (shown in Figure 9) is generally reduced for high Reynolds numbers (above 100), presumably because such conditions are less sensitive to flow perturbations. In addition, it was found that the adjunct drag force (A_D) correlates with rapid temporal variations of V_{rel}, presumably due to increases in flow nonuniformity and unsteadiness. The adjunct lift force (A_L) showed the most significant correlation with the gradient of the surrounding liquid velocity (Figure 10) and to a lesser extent with the surrounding liquid vorticity. This is attributed to when the bubbles move to regions of high vorticity or high velocity gradient where the flowfield is typically more nonuniform, that is, strong variations in ∇V_L exist within the area integral of Eq. 7, and the quasi-steady predictions are no longer consistently valid. Other correlations studies of the adjunct lift force showed that its absolute value increases with the absolute value of S_L and the average liquid perturbation velocity around the bubble, q'_L. Thus, some qualitative tendencies of the forces not accounted for by traditional point

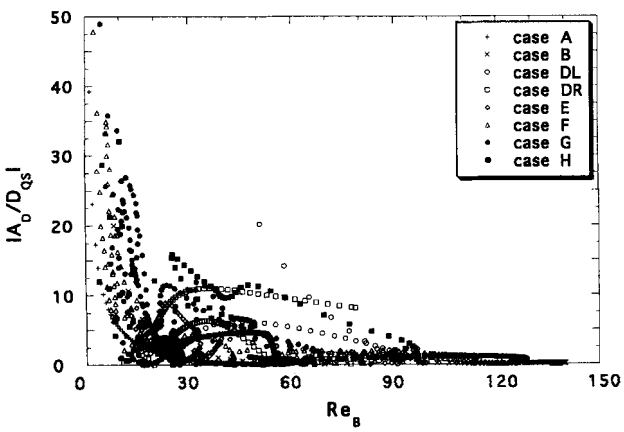

Figure 9. Absolute value of the adjunct force in the drag direction (normalized by the quasi-steady drag) vs. the bubble Reynolds number for cases A–H.

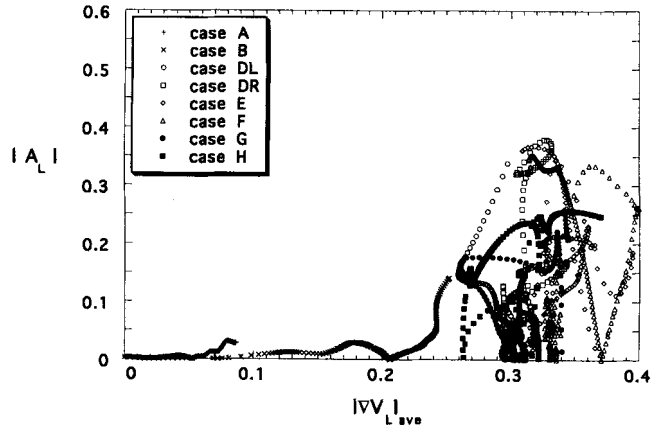

Figure 10. Absolute value of the adjunct force in the lift direction vs. the absolute value of the average velocity gradient of the liquid around the bubble for cases A–H.

bubble equations have been noted. In the future, we hope to develop and test specific models for the adjunct forces (based on physical reasoning and statisical correlations with the unsteady features of the turbulent flowfield) to provide a more accurate description of bubble hydrodynamic forces in complex bubbly flows for potential use in point bubble computations. Such models may include a statistically fluctuating component of the adjunct forces to mimic their oscillatory behavior about the quasi-steady forces.

Conclusions

The present study investigated the hydrodynamic forces for a large cylindrical bubble embedded in a planar free shear layer. By solving the detailed flow around and inside the bubble, the DNS hydrodynamic forces and trajectories could be compared with those expected from quasi-steady classical predictions. This led to the following observations. Bubble dispersion based on a point bubble approximation was much different from that based on large bubble DNS calculations, due to modification of bubble hydrodynamic forces in both the lift and drag directions. Based on the DNS force evolutions, the adjunct drag force was found to correlate with regions of high relative velocity and its time derivative, such as found near the braid centers, where increases in flow nonuniformity and unsteadiness were present. Significant adjunct lift forces were correlated with local regions of high surrounding liquid velocity fluctuation, flow divergence, and stress gradient, such as found near the eddy cores. In addition, the instantaneous adjunct force exhibited strong fluctuations, but these deviations were both negative and positive such that their time average values were low. Finally, it appeared that the variations in the added mass coefficient are only sufficient to explain a minority of the effects caused by the nonlinear spatial and temporal gradients of the surrounding liquid.

Acknowledgments

This work was supported by the Office of Naval Research (ONR) under contract N00014-92-J-1157 with Dr. Edwin Rood as technical

monitor. The National Center for Supercomputing Applications (NCSA) at the University of Illinois at Urbana-Champaign (UIUC), under grant CBT920031N, furnished the Cray computer time used for the numerical calculations. We wish to acknolwedge Professor Gretar Tryggvason of the University of Michigan who originally developed the single-fluid two-phase flow code and provided valuable counseling. Also, the help of Mr. James Lin and Mr. Sean Freeburger (B.S. in Aeronautical and Astronautical Engineering Dept. at UIUC) in flow visualization and data reduction is acknowledged.

Notation

A = bubble adjunct force vector
C_m = bubble added mass coefficient
g = acceleration due to gravity
r = distance from bubble centroid
t = time normalized by $2\delta_{\omega 0}/u_1$
$\Delta u = u_1 - u_2 = 2u_1$
V = velocity
Vol = volume
Δx = grid spacing
X = position vector (x in streamwise direction and y in transverse direction)

Subscripts and superscripts

$()_0$ = initial condition at $t = 0$
$()^f$ = conditions along front
$()'$ = nonnormalized force or perturbation quantity

Literature Cited

Auton, T. R., J. C. R. Hunt, and M. Prud'Homme, "The Force Exerted on a Body in Inviscid Unsteady Non-Uniform Rotational Flow," *J. Fluid Mech.*, **197**, 241 (1988).

Bhaga, D., and M. E. Weber, "Bubbles in Viscous Liquids: Shapes, Wakes and Velocities," *J. Fluid Mech.*, **105**, 61 (1981).

Cebrzynski, M. S., and E. Loth, "Modulation of Shear Layer Thickness Due to Large Bubbles," *Int. J. Multiphase Flow*, submitted (1994).

Faeth, G. M., "Mixing, Transport, and Combustion in Sprays," *Prog. Energy Combust. Sci.*, **13**, 293 (1987).

Jiang, R. L., R. L. Varty, and L. W. Sigurdson, "The Acceleration of a Single Bubble Rising from a Nozzle in Water," *ASME, Gas-Liquid Flows*, **FED 165**, 161 (1993).

Kuo, J. T., and G. B. Wallis, "Flow of Bubbles Through Nozzles," *Int. J. Multiphase Flow*, **14** (5), 547 (1988).

Maxey, M. R., and J. J. Riley, "Equation of Motion for a Small Rigid Sphere in a Non-Uniform Flow," *Phys. Fluids*, **26**(4), 883 (1983).

Mei, R., C. J. Lawrence, and R. J. Adrian, "Unsteady Drag on a Sphere at Finite Reynolds Number with Small Fluctuations in the Free-Stream Velocity," *J. Fluid Mech.*, **233**, 613 (1991).

Mei, R., J. F. Klausner, and C. J. Lawrence, "A Note on the History Force on a Spherical Bubble at Finite Reynolds Number," *Phys. Fluid*, **6**(1), 418 (1994).

Metcalfe, R. W., S. A. Orszag, M. E. Brachet, S. Menon, and J. J. Riley, "Secondary Instability of a Temporally Growing Mixing Layer," *J. Fluid Mech.*, **184**, 207 (1987).

Oakley, T., E. Loth, and R. J. Adrian, "Cinematic Particle Image Velocimetry of a Turbulent Free Shear Layer," AIAA-94-2298 (1994).

Odar, F., and W. Hamilton, "Forces on a Sphere Accelerating in a Viscous Fluid," *J. Fluid Mech.*, **18**, 302 (1964).

Ruetsch, G. R., and E. Meiburg, "On the Motion of Small Spherical Bubbles in Two-Dimensional Vortical Flows," *Phys. Fluids A*, **5** (10), 2326 (1993).

Sangani, A. S. and A. K. Didwania, "Dynamic Simulations of Flows of Bubbly Liquid at Large Reynolds Numbers," *J. Fluid Mech.*, **250**, 307 (1993).

Shankar, P. N., "On the Shape of a Two-Dimensional Bubble in Uniform Motion," *J. Fluid Mech.*, **244**, 187 (1992).

Sherman, F. S., *Viscous Flow*, McGraw-Hill, New York (1990).

Soo, S. L., "Net Effect of Pressure Gradient on a Sphere," *Phys. Fluids*, **19** (5), 757 (1976).

Sridhar, G. and J. Katz, "Lift and Drag Forces on Bubbles Entrained by a Vortex Ring," *ASME, Cavitation Multiphase Flow Forum*, **FED 153**, 165 (1993).

Taeibi-Rahni, M., E. Loth, and G. Tryggvason, "Flow Modulation of a Planar Free Shear Layer with Large Bubbles—Direct Numerical Simulations," *Int. J. Multiphase Flow*, **20**(6), 1109 (1994).

Taeibi-Rahni, M. "Direct Numerical Simulations of Large Bubbles in a Free Shear Layer," PhD Diss., Dept. of Aeronautical and Astronautical Engineering, Univ. of Illinois at Urbana-Champaign, Urbana (1995).

Tio, K.-K., J. C. Lasheras, A. M. Gañán-Calvo, and A. Liñán, "The Dynamics of Bubbles in Periodic Vortex Flows," *J. Appl. Sci. Res.*, **51**, 285 (1993).

Tsuboi, K., T. Tamura, and K. Kuwahara, "Numerical Study for Vortex Induced Vibration of a Circular Cylinder in High Reynolds Number Flow," AIAA-89-0294 (1989).

Unverdi, S. O., and G. Tryggvason, "A Front-Tracking Method For Viscous, Incompressible, Multi-Fluid Flows," *J. Comp. Phys.*, **100**(1), 25 (1992).

White, F. M. *Viscous Fluid Flow*, 2nd ed., McGraw-Hill, New York (1991).

Yang, Y., and L. G. Leal, "A Note on Memory-Integral Contributions to the Force on an Accelerating Spherical Drop at Low Reynolds Number," *Phys. Fluids A*, **3**(7), 1822 (1991).

Manuscript received Oct. 28, 1994, and revision received Mar. 9, 1995.